

Magnetic structure and excitations of the topological semimetal YbMnBi₂

Jian-Rui Soh,¹ Henrik Jacobsen,¹ Bachir Ouladdiaf,² Alexandre Ivanov,² Andrea Piovano,² Tim Tejsner,^{2,3} Zili Feng,⁴ Hongyuan Wang,^{5,6} Hao Su,⁵ Yanfeng Guo,⁵ Youguo Shi,⁴ and Andrew T. Boothroyd^{1,*}

¹*Department of Physics, University of Oxford, Clarendon Laboratory, Parks Road, Oxford OX1 3PU, UK*

²*Institut Laue-Langevin, 6 rue Jules Horowitz, 38042 Grenoble Cedex 9, France*

³*Nanoscience Center, Niels Bohr Institute, University of Copenhagen, DK-2100 Copenhagen, Denmark*

⁴*Beijing National Laboratory for Condensed Matter Physics,*

Institute of Physics, Chinese Academy of Sciences, Beijing 100190, China

⁵*School of Physical Science and Technology, ShanghaiTech University, Shanghai 201210, China*

⁶*University of Chinese Academy of Sciences, Beijing 100049, China*

(Dated: October 31, 2021)

We investigated the magnetic structure and dynamics of YbMnBi₂, with elastic and inelastic neutron scattering, to shed light on the topological nature of the charge carriers in the antiferromagnetic phase. We confirm C-type antiferromagnetic ordering of the Mn spins below $T_N = 290$ K, and determine that the spins point along the c -axis to within about 3°. The observed magnon spectrum can be described very well by the same effective spin Hamiltonian as was used previously to model the magnon spectrum of CaMnBi₂. Our results show conclusively that the creation of Weyl nodes in YbMnBi₂ by the time-reversal-symmetry breaking mechanism can be excluded in the bulk.

PACS numbers: 75.25.-j, 75.30.Ds, 75.30.Gw, 74.70.Xa

I. INTRODUCTION

Dirac and Weyl materials are semimetals whose valence and conduction bands have a linear dispersion in the vicinity of the Fermi energy^{1,2}. These gapless band crossings, which are protected by topology or crystalline symmetries, can give rise to massless quasi-particle excitations which can be described by the relativistic Dirac or Weyl equations. Materials that host such fermions possess a range of desirable physical properties: exceptionally high electrical and thermal conductivities, immunity to disorder and ballistic electronic transport^{3–5}.

Weyl semimetals (WSMs) can occur in crystals with broken spatial inversion symmetry (IS), broken time-reversal symmetry (TRS), or both. Examples of the first type (with broken IS only) were found in 2015^{6–9}, but realizations of WSMs with broken TRS are still rare². Recently, the layered AFM YbMnBi₂ was proposed as a potential candidate¹⁰. The evidence from angle-resolved photoemission spectroscopy (ARPES) is quite convincing¹⁰, and there is also some support from optics^{11,12}.

The tetragonal unit cell of YbMnBi₂, which can be described by the $P4/nmm$ space group (No. 129), includes alternating Bi square layers that host the possible Weyl fermions,^{10–16} and MnBi₄ tetrahedral layers which contain magnetic moments on the Mn atoms [See Fig. 1(a)]. In the antiferromagnetically (AFM) ordered phase, below $T_N = 290$ K, neighbouring Mn spins are reported to be antiparallel within the ab plane, but crucially, they are ferromagnetically stacked along the c -axis^{14,15,17}. This means that magnetic coupling to the Bi conduction states is allowed at the mean-field level, which can lead to band splitting.

In Ref. 10, it was argued that creation of Weyl points by TRS breaking in YbMnBi₂ requires a $\sim 10^\circ$ canting of the Mn moments away from the c -axis. If present, this

canting would generate a net ferromagnetic component in the ab -plane of YbMnBi₂, and would account for the Weyl nodes and arcs observed in the ARPES data. Such a small deviation in the moment direction from the c -axis would not have been discernible in the (100) magnetic peak studied in the previous neutron diffraction measurements^{14,15,17}, so the possibility that YbMnBi₂ might be a WSM by this mechanism remains to be tested.

Moreover, if the AFM order of manganese creates Weyl fermions, which then dominate the electronic transport^{14,15}, then these quasiparticle excitations could play be expected to play some role in the exchange coupling between Mn moments which could in turn influence the magnon spectrum. As the magnetic order is key to the behavior of YbMnBi₂ as a topological material, measurements of the magnon spectrum, and the exchange parameters derived from it, could provide additional information on the presence of Weyl fermions near the Fermi energy.

In light of this, we set out in this study, (i) to search for evidence of a canted magnetic structure by neutron diffraction, and (ii) to investigate the magnon spectrum in the AFM phase of YbMnBi₂ through inelastic neutron scattering. To achieve the required sensitivity to the predicted ferromagnetic component of the proposed canted magnetic structure, we performed careful measurements of the weak (00 l) nuclear reflections. Furthermore, to identify any anomalies in the magnetic exchange between Mn moments associated with the presence of Weyl fermions, we compare the observed magnon spectrum with that of Dirac semimetal CaMnBi₂¹⁸, which is isostructural to YbMnBi₂. We demonstrate that the Mn sublattice in YbMnBi₂ has C-type AFM ordering below $T_N = 290$ K, with the moments aligned along the c -axis to within 3° (at 95% confidence level). Moreover, we find no evidence from the magnon spectrum for anomalous mag-

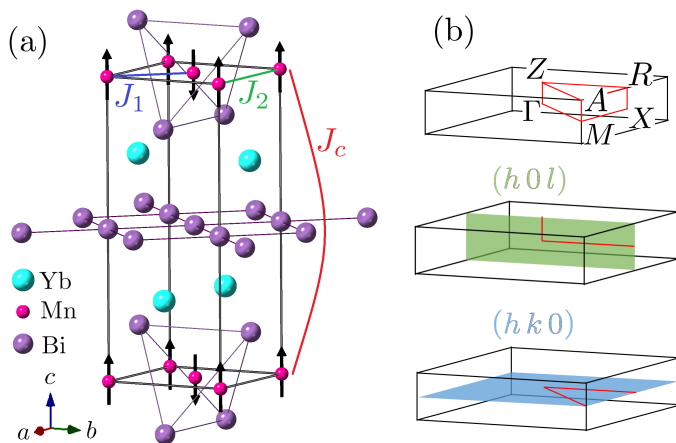


FIG. 1. (a) The unit cell of YbMnBi₂ for the space group *P4/nmm* (No. 129). The proposed Weyl fermions are contained in the Bi square net in the center of the unit cell. The magnetic exchange between the *ab*-plane nearest neighbor (*J*₁), *ab*-plane next-nearest neighbor (*J*₂), and *c*-axis nearest neighbor (*J*_{*c*}) Mn²⁺ ions were used in the linear spin-wave model to describe the magnon spectrum. (b) The definition of high symmetry lines and planes in the first Brillouin zone of the tetragonal lattice. The spin-wave spectrum in the *(h0l)* and *(hk0)* reciprocal lattice planes was mapped in this work. Here, the reciprocal lattice vector is defined as, $\mathbf{G} = h\mathbf{b}_1 + k\mathbf{b}_2 + l\mathbf{b}_3$, where $|\mathbf{b}_1| = |\mathbf{b}_2| = 2\pi/a$ and $|\mathbf{b}_3| = 2\pi/c$.

netic coupling between the Mn spins. Our results rule out the existence of magnetically-induced Weyl fermions in the bulk of YbMnBi₂, but leave open the possibility that the $\sim 10^\circ$ canting of the Mn moments needed to form the Weyl nodes might occur at the surface.

II. EXPERIMENTAL DETAILS

Single crystalline YbMnBi₂ was grown by the self-flux method. The starting materials were mixed together in a molar ratio of Yb:Mn:Bi = 1:1:8. The mixture was placed into an alumina crucible, sealed in a quartz tube, then slowly heated to 900°C and kept at this temperature for 10 hours. The assembly was subsequently cooled down to 400°C at a rate of 3°C/hour. It was finally taken out of the furnace at 400°C and was put into a centrifuge immediately to remove the excess Bi. The structure and quality of the single crystals was checked with laboratory x-rays on a 6-circle diffractometer (Oxford Diffraction) and Laue diffractometer (Photonic Science). A superconducting quantum interference device (SQUID) magnetometer (Quantum Design) was used to study the magnetization of YbMnBi₂ as a function of temperature. These zero-field-cooled (ZFC) magnetometry measurements were performed in the temperature range 10 to 370 K in a field of 1 T applied parallel to the *a*- and *c*-axes of YbMnBi₂.

Elastic neutron scattering of a YbMnBi₂ single crystal

with a mass of 76 mg was performed on a 4-circle diffractometer (D10) at the Institut Laue-Langevin (ILL) reactor source. The intensities of the reflections were studied over the temperature range of 20 to 400 K. A pyrolytic graphite (PG) monochromator was used to select the incident neutron wavelength of $\lambda = 2.36 \text{ \AA}$. The rocking curve of each peak was obtained by measuring the number of scattered neutrons at each rocking angle (ω) with a $80 \times 80 \text{ mm}^2$ area detector.

Inelastic neutron scattering measurements were performed on the triple-axis neutron spectrometer IN8¹⁹ with the FlatCone detector²⁰ at the ILL. A YbMnBi₂ single crystal (mass 1 g) was initially oriented with the *a* and *c* crystal axes horizontal to map the spin-wave spectrum in the *(h0l)* scattering plane (see Fig. 1). The crystal was subsequently rotated by 90° (such that the crystalline *a* and *b* axes were in the scattering plane) to access the *(hk0)* plane. Constant-energy maps were measured at various energies, $\Delta E = E_i - E_f$. The outgoing neutron wavevector was fixed at $k_f = 3 \text{ \AA}^{-1}$ ($E_f = 18.6 \text{ meV}$) by elastically-bent Si (111) analyzer crystals, and the required energy transfers were set by selecting the incident wavevector, k_i , with an incident beam monochromator. For energy transfers $\Delta E \geq 40 \text{ meV}$, a PG (002) double-focusing monochromator was used, and for $\Delta E < 40 \text{ meV}$ an elastically-bent, perfect Si (111) double-focusing monochromator was used.

The array of 31 detectors on the FlatCone device allows for the simultaneous acquisition of scattered intensity along arcs in reciprocal space. By rotating the single crystal about the scattering plane normal, these arcs can sweep out areas in *k*-space to give reciprocal space maps.

III. RESULTS AND ANALYSIS

The x-ray diffraction patterns of single crystalline YbMnBi₂ obtained from the 6-circle and Laue diffractometers are fully consistent with the *P4/nmm* space group, with cell parameters $a = 4.4860(13) \text{ \AA}$ and $c = 10.864(4) \text{ \AA}$ (Ref. 21). Moreover, the small mosaic spread in the diffraction peaks ($< 1.24^\circ$) points to a high crystalline quality of the flux-grown crystals.

The temperature dependence of the magnetic susceptibility of YbMnBi₂, with the field applied parallel to the *a* and *c* crystal axes, is shown in Fig. 2(a). The anomaly in the χ_c data at $T_N \simeq 290 \text{ K}$ is associated with the onset of AFM order in the Mn²⁺ sublattice. This value for the Néel temperature is consistent with those reported in earlier studies of YbMnBi₂^{10,14,15}, as well as the neutron diffraction data presented in this work (see later). Below T_N , the magnetic susceptibility becomes strongly anisotropic with respect to applied field, where $\chi_a > \chi_c$. This bifurcation of $\chi(T)$ at T_N suggests that the manganese moments, in the ordered phase, are more susceptible to an in-plane field than a field applied along the *c*-axis, in agreement with earlier reports^{10,14}. At low temperatures (below 50 K), the susceptibility grows in

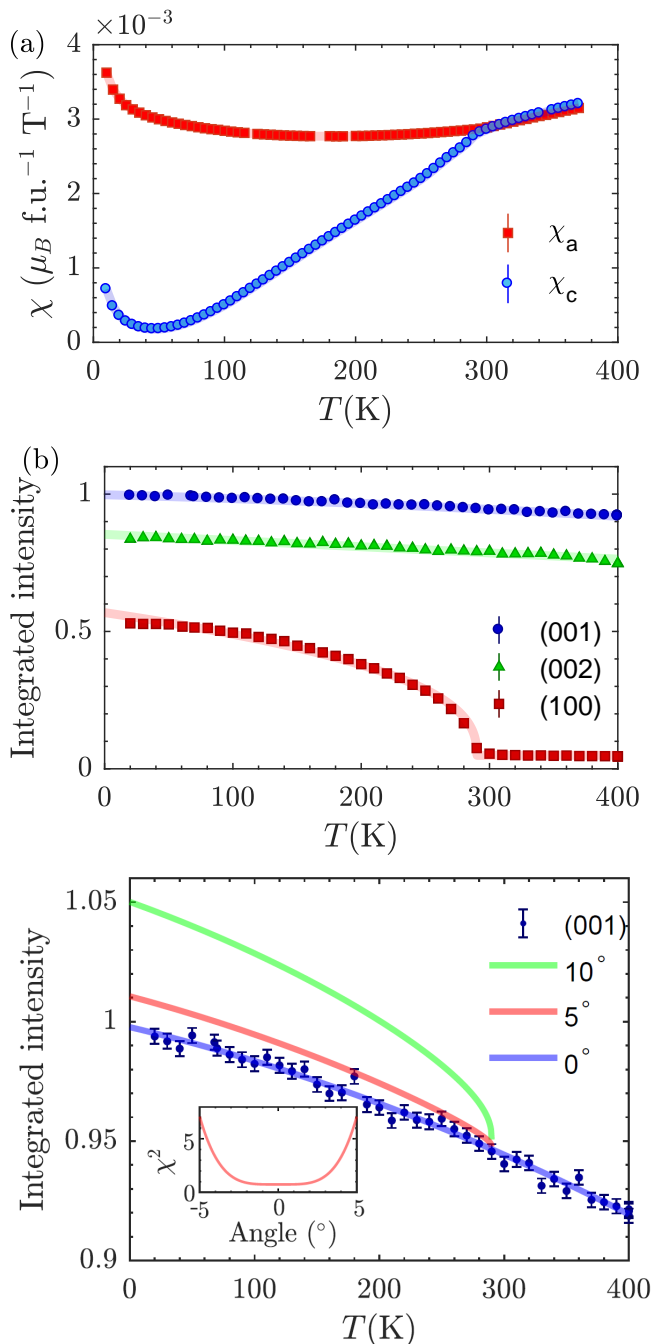


FIG. 2. (a) Temperature dependence of the magnetic susceptibility of YbMnBi₂ measured with the field applied along the *a* and *c* axes (χ_a and χ_c , respectively). The single crystal was cooled in zero field and measured in an applied field strength of 1 T. (b) Temperature dependence of the integrated intensity of the (001), (002) and (100) peaks. The red line is a power law fit to the temperature dependence of the (100) reflection which gives a transition temperature of $T_N = 290(1)$ K. (c) Measured intensity of the (001) peak, together with lines calculated for tilt angles of 0°, 5° and 10°. The inset shows the variation of the χ^2 with tilt angle.

both field directions. This upturn is likely due to a small

concentration of a Mn-containing paramagnetic impurity phase, and is observed in other members of the AMnBi₂ family (*A* = Sr, Ca, Ba)^{22–24}.

A. Elastic Neutron Scattering

Neutron diffraction data in the temperature range 20 to 400 K are presented in Fig. 2(b). As the sample was cooled below $T = 290$ K, the (100) peak, which is otherwise forbidden in the *P4/nmm* space group, was observed. This reflection is consistent with a magnetic propagation vector of $\mathbf{k} = \mathbf{0}$. The onset of this purely magnetic peak at T_N reveals the incipient AFM order of the Mn²⁺ sublattice. The temperature dependence of the integrated peak intensity fits very well to a power law, $I_{obs} \propto |T_N - T|^{2\beta}$, with critical exponent $\beta = 0.38(2)$, consistent with the 3D Heisenberg universality class.

The predicted canting of the Mn²⁺ moments away from the *c*-axis^{10–12} should produce a small *ab*-plane ferromagnetic component. Given that magnetic neutron scattering is sensitive to the component of the ordered moment perpendicular to the scattering vector \mathbf{Q} ,²⁵ we can isolate this small in-plane component by studying the intensity of reflections with $\mathbf{Q} \parallel c$. If there were an in-plane ferromagnetic component then the intensity of (00*l*) peaks should increase on cooling below T_N , as was observed in a sister compound SrMnSb₂²⁶, where a small in-plane ferromagnetic contribution to the nuclear peak was reported²⁷.

To minimize the reduction of the scattered intensity due to the magnetic form factor of Mn²⁺, we studied the reflections with the smallest \mathbf{Q} , namely the (001) and (002) peaks, as shown in Fig. 2(b). We observe no discernible change in the integrated intensity of these peaks apart from the gradual increase with decreasing temperature which can be attributed to the Debye–Waller factor.

In Fig. 2(c) we show the intensity of the (001) peak on a magnified scale, together with lines calculated assuming tilt angles of 0°, 5° and 10°. The 0° curve is a quadratic fit to the data, and the other two curves are obtained by adding the calculated magnetic intensity of the (001) peak to the 0° curve based on the measured intensity of the (100) peak. We also calculated the variation of the χ^2 goodness-of-fit statistic as a continuous function of tilt angle, see inset to Fig. 2(c). From the χ^2 distribution, we find that the probability of a tilt angle greater than 3° is only 5%.

These results imply that the ordered moments in YbMnBi₂ are collinear and aligned along the *c*-axis to within 3° at a 95% confidence level. Hence, a 10° canting of Mn²⁺ moments away from the *c*-axis, as required to create the Weyl nodes, can be excluded.

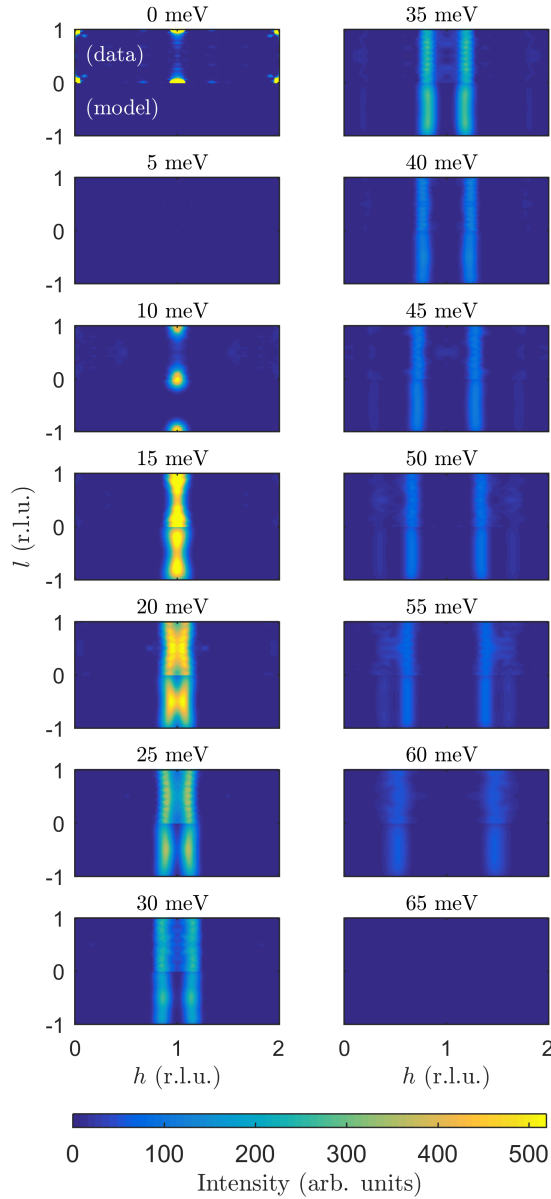


FIG. 3. Constant-energy maps in the $(h0l)$ plane in reciprocal space, illustrated in Fig. 1(b), at various ΔE , plotted in reduced lattice units (r.l.u.). In each panel, the top and bottom half correspond to the data and model, respectively.

B. Inelastic Neutron Scattering

Constant-energy maps of the scattering intensity recorded in the $(h0l)$ and $(hk0)$ reciprocal lattice planes at various energy transfers, ΔE , are shown in Figs. 3 and 4, respectively. We discuss the data from the different scattering planes in turn, starting with the $(h0l)$ data, which appears in the top half of each panel in Fig. 3.

We find the lowest energy spin-wave mode at the Γ point, with an energy gap of $\Delta E \simeq 10$ meV. This gap is caused by the magnetic anisotropy which favors spin

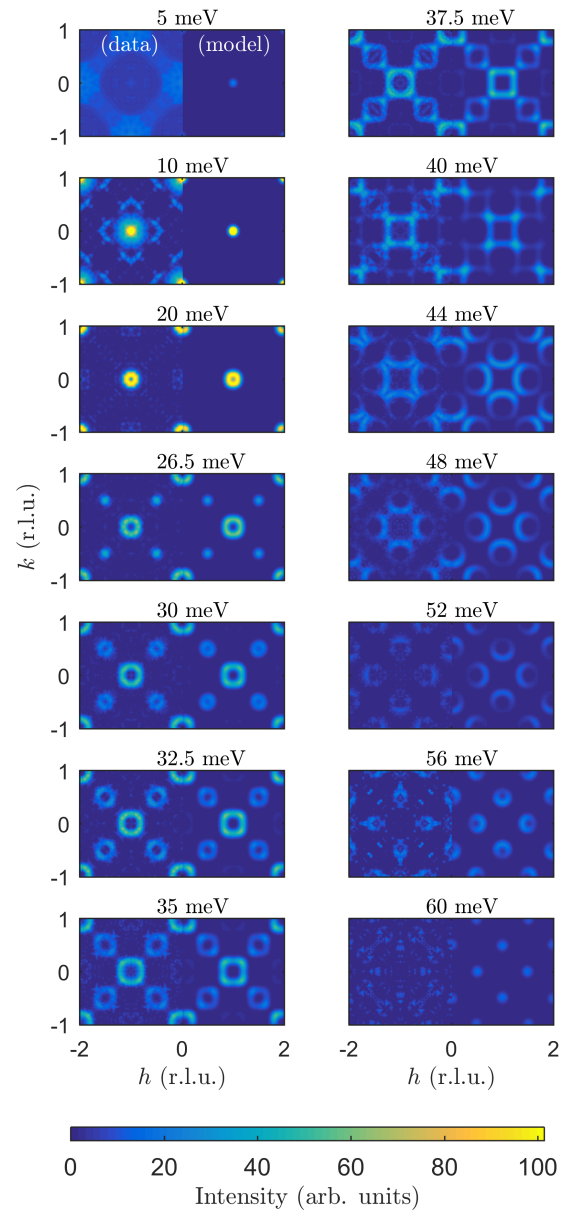


FIG. 4. Constant-energy maps in the $(hk0)$ plane in reciprocal space, illustrated in Fig. 1(b), at various ΔE . In each panel, the left and right half correspond to the data and model, respectively.

alignment along the c axis. At $\Delta E = 20$ meV, we find pinch points in the magnon spectrum at the high symmetry point Z , that is, halfway between Γ points in adjacent Brillouin zones along l . These pinch points form as a result of the dispersion along the c -axis. For $\Delta E \geq 30$ meV, the magnon dispersion along l goes away, and the intensity becomes independent of l . In other words, the Mn spin dynamics becomes two-dimensional. The spectrum reaches a maximum along the $R-X-R$ high symmetry line at $\Delta E = 60$ meV.

We now turn to the reciprocal space maps in the $(hk0)$ scattering plane at various energy transfers, which corre-

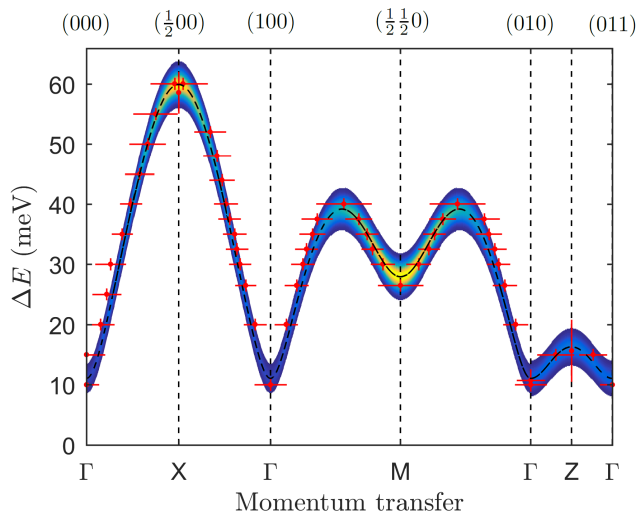


FIG. 5. The observed and calculated spin-wave spectrum of the Mn spins in YbMnBi₂ along high symmetry directions, as defined in Fig. 1(b). The calculated magnon spectrum is in good agreement with the measured spin-wave dispersion (red markers), which was obtained from constant-energy cuts through the intensity maps in the (*h*0*l*) and (*h**k*0) planes.

spond to the left half of each panel in Fig. 4. Just as in the (*h*0*l*) plane, we observe the lowest energy excitations at the Γ point in the Brillouin zone at $\Delta E = 10$ meV. For $10 \leq \Delta E \leq 26.5$ meV, the spectrum develops into rings centered at Γ , which is characteristic of isotropically dispersing spin waves in the *ab* plane. At $\Delta E = 26.5$ meV, we observe a saddle in the spin-wave spectrum appearing at the high symmetry point *M*. The maximum in the dispersion is once again found at the *X* point, at $\Delta E \leq 60$ meV.

To obtain the spin-wave dispersion, cuts were made along the $Z - \Gamma - X$ and $M - \Gamma - X$ high symmetry lines [see Fig. 1(b)] through the measured intensity maps in the (*h*0*l*) and (*h**k*0) planes, respectively. The intensity in cuts at various ΔE was fitted with peak functions to identify the magnon wavevectors for each ΔE . In Fig. 5 we present the measured spin-wave dispersion determined this way.

In order to model the observed magnon spectrum we employed the effective spin Hamiltonian

$$\mathcal{H} = \sum_{i,j} J_{ij} \mathbf{S}_i \cdot \mathbf{S}_j - \sum_i D(S_i^z)^2, \quad (1)$$

where J_{ij} is the (isotropic) exchange between Mn spins \mathbf{S}_i and \mathbf{S}_j on sites *i* and *j*, and *D* is a single-ion anisotropy parameter making the *c* axis an easy axis. In the first summation, we include first and second nearest neighbors in the *ab* plane (J_1 and J_2), and nearest neighbors along the *c* axis (J_c). We used linear spin-wave theory as implemented in the SpinW software²⁸ to calculate the magnon spectrum.

By fitting the linear spin-wave model to the measured dispersion we find values for the parameters SJ_1

$= 22.6(5)$ meV, $SJ_2 = 7.8(5)$ meV, $SJ_c = -0.13(5)$ meV and $SD = 0.37(4)$ meV (see Supplemental Material for details²¹), where *S* is the spin quantum number, which for Mn²⁺ is $S = 5/2$. Based on these parameters, we present the calculated constant-energy intensity maps in the (*h*0*l*) and (*h**k*0) planes on the lower and right halves of the panels in Figs. 3 and 4, respectively, and we plot the calculated magnon spectrum along high symmetry directions in Fig. 5. Overall, we find that the calculated spectrum agrees very well with the data.

IV. DISCUSSION

As neutron diffraction probes the entire volume of the sample, our results rule out the possibility of magnetically-induced Weyl nodes in the bulk of YbMnBi₂. On the other hand, neutron diffraction would not be sensitive to a canting of the magnetic moments at the surface of the sample. Such a canting, if present, would reconcile the results of the present study with the work by Borisenko *et al.*¹⁰.

In YbMnBi₂, the spontaneous magnetic order in the Mn sublattice coexists with massless quasiparticle excitations arising from the Bi square net. Armed with the best-fit parameters of the linear spin-wave model, we are now in the position to address whether the magnon spectrum in YbMnBi₂ differs in any detectable way compared with other related systems. For instance, one might expect to see differences in the inter-layer exchange coupling parameter J_c if the conducting states on the Bi layers were very unusual in YbMnBi₂.

To elucidate this, we compare the fitted spin-wave model parameters obtained in this work with those of CaMnBi₂, which is isostructural to YbMnBi₂. CaMnBi₂ possesses a near identical Néel temperature to YbMnBi₂ of $T_N = 290$ K,^{18,22} and is predicted to be a Dirac semimetal.^{29–31} Using the same Hamiltonian (1), the three magnetic exchange parameters in CaMnBi₂ were found to be $SJ_1 = 23.4(6)$ meV, $SJ_2 = 7.9(5)$ meV and $SJ_c = -0.10(5)$ meV,¹⁸ which are the same as those of YbMnBi₂ to within experimental error. The anisotropy parameter for CaMnBi₂, $SD = 0.18(3)$ meV, is about half that for YbMnBi₂, which reflects that the energy gap at Γ is slightly smaller in CaMnBi₂ than in YbMnBi₂. These results demonstrate that the magnon spectrum of YbMnBi₂ does not show any anomalous behavior relative to that of CaMnBi₂.

More broadly, this suggests that replacing the divalent alkali-earth metal Ca²⁺ on the *A* site of AMnBi₂ with the rare-earth Yb²⁺ ion does not significantly enhance the coupling between the magnetism in the octahedral MnBi₄ layers and the charge carriers in the Bi square net. This is despite the fact that the *A* atom is situated along the direct exchange path between the Mn and Bi atoms. In a recent review of the wider AMn*Pn*₂ family of compounds, Klemenz *et al.*¹³ suggested another route to enhance the coupling between magnetism and the topological charge

carriers, namely to have a magnetic ion on the A site (like Eu^{2+}) rather than non-magnetic ions such as Ca^{2+} , Sr^{2+} , Ba^{2+} and Yb^{2+} . This was prompted by the fact that the A site atom is in closer proximity to the square Bi compared to the Mn^{2+} ion and might lead to a greater orbital overlap and thus magnetic exchange interaction. In fact, this was considered in Refs. 10 and 12, where the electronic structure and optical properties of EuMnBi_2 and YbMnBi_2 were compared. The divalent rare-earth ions on the A site of both AMnBi_2 compounds have comparable ionic radius and very similar relative positions to the Bi square layer, but with the difference that Eu^{2+} has half-filled $4f$ orbitals compared to the fully-filled case for Yb^{2+} . This leads to a large pure-spin magnetic moment of $7\mu_B$ on the A site of EuMnBi_2 , and a non-magnetic ion on the A site of YbMnBi_2 . These studies demonstrate a marked increase in coupling between magnetism and the topological charge carriers in EuMnBi_2 compared to that in YbMnBi_2 , which is consistent with magnetotransport studies^{10,14,32–34}. This suggests that in EuMnBi_2 , compared to YbMnBi_2 , a greater coupling of magnetism to the pnictide square net can be achieved with magnetic species on the A site, which for the extended AMnPn_2 (or 112-pnictide) family, is closer to the pnictide layer compared to Mn.

Finally, it is instructive to compare the physical properties of YbMnBi_2 with that of YbMnSb_2 , which is isostructural to YbMnBi_2 ^{35,36} and also exhibits Mn AFM order with a similar magnetic ordering temperature of $T_N = 345\text{ K}$. A comparison of the band structures of the two 112 pnictides reveal a greater extent of inversion in the conduction and valence bands in YbMnBi_2 , with several band crossings at E_F as shown Refs. 10 and 11, compared to that in YbMnSb_2 .³⁶ Moreover, the Shubnikov–de Haas (SdH) oscillation of the magnetotransport in both compounds reveals that the effective mass of the charge carriers in YbMnBi_2 ($m_c^* \sim 0.24 m_e$ ¹⁵) is approximately twice that of YbMnSb_2 as reported in Refs. 35 and 36.

These features can be understood from the relative sizes of the spin–orbit coupling (SOC) in the pnictide square conducting layers, which is significantly larger in YbMnBi_2 as Bi is ~ 1.7 times heavier than Sb. Given that the linear band crossing along the Γ – M high symmetry line is not protected by symmetry, the doubly-degenerate pnictide (Sb $5p$ or Bi $6p$) bands hybridize and give rise to an avoided Dirac crossing. As such, the stronger SOC in YbMnBi_2 produces a larger energy gap in the electronic bands, resulting in a heavier effective mass of the charge carriers compared to that in YbMnSb_2 . This is consistent with the work in Ref. 37, which explored the effect of the masses of pnictides on the physical properties of BaMnPn_2 ($\text{Pn} = \text{Sb}, \text{Bi}$). In that work, Liu *et al.* also proposed that a more suitable platform to realize massless Dirac fermions is in replac-

ing Bi with lighter elements in the same group. This demonstrates that the 112 pnictide family of compounds offers strong tunability of the effective mass of the charge carriers from the size of the SOC.

V. CONCLUSION

We have presented the magnetic structure and magnon spectrum of the candidate Weyl semimetal YbMnBi_2 . The $(00l)$ family of nuclear reflections does not display any additional magnetic contribution below T_N , and this rules out the mechanism for creation of Weyl nodes via TRS-breaking through canting of the Mn spins. Hence, we demonstrate that bulk YbMnBi_2 is a Dirac semimetal rather than a host for the WSM state. We have not ruled out the possibility of spin canting at the surface, which could reconcile the present results with those of Ref. 10. The lack of any anomalous features in the magnon spectrum implies a weak coupling between magnetism and the topological charge carriers. YbMnBi_2 belongs to the wider AMnPn_2 family of compounds which are currently attracting strong interest owing to its strong potential for spintronic applications. We hope that the understanding of YbMnBi_2 achieved here will contribute to the development of strategies for enhancing the exchange coupling between charge transport and magnetism, and for reducing the effective mass of the quasiparticles.

ACKNOWLEDGMENTS

The authors wish to thank D. Prabhakaran and F. Charpenay for technical assistance, and M. Newport for fabricating the Al mount used in the INS experiment. We are also grateful to M. C. Rahn and P. Steffens for the data analysis software, P. Manuel and D. D. Khalyavin for help with preliminary neutron studies on WISH, ISIS (beamtime RB1720113), M. Gutmann for checking the single crystal quality of YbMnBi_2 on SXD, ISIS and N. Qureshi for orienting the crystal for the INS experiment on OrientExpress³⁸, ILL (beamtime EASY-365). The D10 and IN8 experiment numbers were DIR-159 and 4-01-1572³⁹ respectively. This work was supported by the U.K. Engineering and Physical Sciences Research Council, Grant Nos. EP/N034872/1 and EP/M020517/1, the Natural Science Foundation of Shanghai (Grant No. 17ZR1443300), the Shanghai Pujiang Program (Grant No. 17PJ1406200), the National Key Research and Development Program of China (Grant No. 2017YFA0302901), the Beijing Natural Science Foundation (Grant No. Z180008) and the K. C. Wong Education Foundation (Grant No. GJTD-2018-01). J.-R. Soh acknowledges support from the Singapore National Science Scholarship, Agency for Science Technology and Research.

- * andrew.boothroyd@physics.ox.ac.uk
- ¹ A. A. Burkov, Nat. Mat. **15**, 1145 (2016).
 - ² N. P. Armitage, E. J. Mele, and A. Vishwanath, Rev. Mod. Phys. **90**, 015001 (2018).
 - ³ J. G. Rau, E. K.-H. Lee, and H.-Y. Kee, Ann. Rev. Con. Mat. Phys. **7**, 195 (2016).
 - ⁴ D. Pesin and L. Balents, Nat. Phys. **6**, 376 (2010).
 - ⁵ M. Z. Hasan and C. L. Kane, Rev. Mod. Phys. **82**, 3045 (2010).
 - ⁶ B. Q. Lv, H. M. Weng, B. B. Fu, X. P. Wang, H. Miao, J. Ma, P. Richard, X. C. Huang, L. X. Zhao, G. F. Chen, Z. Fang, X. Dai, T. Qian, and H. Ding, Phys. Rev. X **5**, 031013 (2015).
 - ⁷ S.-M. Huang, S.-Y. Xu, I. Belopolski, C.-C. Lee, G. Chang, B. Wang, N. Alidoust, G. Bian, M. Neupane, C. Zhang, S. Jia, A. Bansil, H. Lin, and M. Z. Hasan, Nat. Comms. **6**, 7373 (2015).
 - ⁸ S.-Y. Xu, I. Belopolski, N. Alidoust, M. Neupane, G. Bian, C. Zhang, R. Sankar, G. Chang, Z. Yuan, C.-C. Lee, S.-M. Huang, H. Zheng, J. Ma, D. S. Sanchez, B. Wang, A. Bansil, F. Chou, P. P. Shibayev, H. Lin, S. Jia, and M. Z. Hasan, Sci. **349**, 613 (2015).
 - ⁹ L. X. Yang, Z. K. Liu, Y. Sun, H. Peng, H. F. Yang, T. Zhang, B. Zhou, Y. Zhang, Y. F. Guo, M. Rahn, D. Prabhakaran, Z. Hussain, S.-K. Mo, C. Felser, B. Yan, and Y. L. Chen, Nat. Phys. **11**, 728 (2015).
 - ¹⁰ S. Borisenko, D. Evtushinsky, Q. Gibson, A. Yaresko, K. Koepernik, T. Kim, M. Ali, J. van den Brink, M. Hoesch, A. Fedorov, E. Haubold, Y. Kushnirenko, I. Soldatov, R. Schäfer, and R. J. Cava, Nat. Comms **10**, 3424 (2019).
 - ¹¹ D. Chaudhuri, B. Cheng, A. Yaresko, Q. D. Gibson, R. J. Cava, and N. P. Armitage, Phys. Rev. B **96**, 075151 (2017).
 - ¹² M. Chinotti, A. Pal, W. J. Ren, C. Petrovic, and L. Degiorgi, Phys. Rev. B **94**, 245101 (2016).
 - ¹³ S. Klemenž, S. Lei, and L. M. Schoop, Annu. Rev. Mater. Res. **49**, 185 (2019).
 - ¹⁴ A. Wang, I. Zaliznyak, W. Ren, L. Wu, D. Graf, V. O. Garlea, J. B. Warren, E. Bozin, Y. Zhu, and C. Petrovic, Phys. Rev. B **94**, 165161 (2016).
 - ¹⁵ J. Y. Liu, J. Hu, D. Graf, T. Zou, M. Zhu, Y. Shi, S. Che, S. M. A. Radmanesh, C. N. Lau, L. Spinu, H. B. Cao, X. Ke, and Z. Q. Mao, Nat. Comms. **8**, 646 (2017).
 - ¹⁶ A. Pal, M. Chinotti, L. Degiorgi, W. Ren, and C. Petrovic, Physica B **536**, 64 (2018).
 - ¹⁷ I. A. Zaliznyak, A. T. Savici, V. O. Garlea, B. Winn, U. Filges, J. Schneeloch, J. M. Tranquada, G. Gu, A. Wang, and C. Petrovic, J. Phys.: Conf. Ser. **862**, 012030 (2017).
 - ¹⁸ M. C. Rahn, A. J. Princep, A. Piovano, J. Kulda, Y. F. Guo, Y. G. Shi, and A. T. Boothroyd, Phys. Rev. B **95**, 134405 (2017).
 - ¹⁹ A. Hiess, M. Jiménez-Ruiz, P. Courtois, R. Currat, J. Kulda, and F. Bermejo, Physica B **385-386**, 1077 (2006).
 - ²⁰ M. Kempa, B. Janousova, J. Saroun, P. Flores, M. Boehm, F. Demmel, and J. Kulda, Physica B **385-386**, 1080 (2006).
 - ²¹ m. m. see supplemental material at <http://link.aps.org/supplemental/10.1103/PhysRevB.00.000000> for laboratory x-ray diffraction patterns and data analysis methods.
 - ²² Y. F. Guo, A. J. Princep, X. Zhang, P. Manuel, D. Khalyavin, I. I. Mazin, Y. G. Shi, and A. T. Boothroyd, Phys. Rev. B **90**, 075120 (2014).
 - ²³ L. Li, K. Wang, D. Graf, L. Wang, A. Wang, and C. Petrovic, Phys. Rev. B **93**, 115141 (2016).
 - ²⁴ Y.-Y. Wang, Q.-H. Yu, and T.-L. Xia, Chin. Phys. B **25**, 107503 (2016).
 - ²⁵ G. L. Squires, *Introduction to the Theory of Thermal Neutron Scattering*, 3rd ed. (Cambridge University Press, 2012).
 - ²⁶ J. Y. Liu, J. Hu, Q. Zhang, D. Graf, H. B. Cao, S. M. A. Radmanesh, D. J. Adams, Y. L. Zhu, G. Cheng, X. Liu, W. A. Phelan, J. Wei, M. Jaime, F. Balakirev, D. A. Tennant, J. F. DiTusa, I. Chiorescu, L. Spinu, and Z. Q. Mao, Nat. Mat. **16**, 905 (2017).
 - ²⁷ Note that the a and c axis in Ref. 26 are interchanged with respect to those defined in the present work. SrMnBi₂ suffers from an off stoichiometry and is better described by Sr_{1-y}Mn_{1-z}Sb₂ ($y, z < 0.1$).
 - ²⁸ S. Toth and B. Lake, J. Phys.: Condens. Matter **27**, 166002 (2015).
 - ²⁹ Y. Feng, Z. Wang, C. Chen, Y. Shi, Z. Xie, H. Yi, A. Liang, S. He, J. He, Y. Peng, X. Liu, Y. Liu, L. Zhao, G. Liu, X. Dong, J. Zhang, C. Chen, Z. Xu, X. Dai, Z. Fang, and X. J. Zhou, Sci. Rep. **4**, 5385 (2014).
 - ³⁰ K. Wang, D. Graf, L. Wang, H. Lei, S. W. Tozer, and C. Petrovic, Phys. Rev. B **85**, 041101(R) (2012).
 - ³¹ A. Zhang, C. Liu, C. Yi, G. Zhao, T.-l. Xia, J. Ji, Y. Shi, R. Yu, X. Wang, C. Chen, and Q. Zhang, Nat. Comms. **7**, 13833 (2016).
 - ³² A. F. May, M. A. McGuire, and B. C. Sales, Phys. Rev. B **90**, 075109 (2014).
 - ³³ H. Masuda, H. Sakai, M. Tokunaga, Y. Yamasaki, A. Miyake, J. Shiogai, S. Nakamura, S. Awaji, A. Tsukazaki, H. Nakao, Y. Murakami, T.-h. Arima, Y. Tokura, and S. Ishiwata, Sci. Adv. **2**, e1501117 (2016).
 - ³⁴ H. Masuda, H. Sakai, M. Tokunaga, M. Ochi, H. Takahashi, K. Akiba, A. Miyake, K. Kuroki, Y. Tokura, and S. Ishiwata, Phys. Rev. B **98**, 161108(R) (2018).
 - ³⁵ Y.-Y. Wang, S. Xu, L.-L. Sun, and T.-L. Xia, Phys. Rev. Mater. **2**, 021201 (2018).
 - ³⁶ R. Kealhofer, S. Jang, S. M. Griffin, C. John, K. A. Benavides, S. Doyle, T. Helm, P. J. W. Moll, J. B. Neaton, J. Y. Chan, J. D. Denlinger, and J. G. Analytis, Phys. Rev. B **97**, 045109 (2018).
 - ³⁷ J. Y. Liu, J. Hu, H. Cao, Y. Zhu, A. Chuang, D. Graf, D. J. Adams, S. M. A. Radmanesh, L. Spinu, I. Chiorescu, and Z. Q. Mao, Sci. Rep. **6**, 30525 (2016).
 - ³⁸ B. Ouladdiaf, J. Archer, G. McIntyre, A. Hewat, D. Brau, and S. York, Physica B **385-386**, 1052 (2006).
 - ³⁹ A. T. Boothroyd, A. Ivanov, H. Jacobsen, A. Piovano, and J.-R. Soh, (2018), 10.5291/ILL-DATA.5-41-975.
 - ⁴⁰ A. F. May, M. A. McGuire, and B. C. Sales, Phys. Rev. B **90**, 075109 (2014).